

Article

Design and Experimental Evaluation of a Single-Actuator Continuous Hopping Robot Using the Geared Symmetric Multi-Bar Mechanism

Long Bai ^{1,*}, Fan Zheng ¹, Xiaohong Chen ¹, Yuanxi Sun ¹ and Junzhan Hou ²

¹ State Key Laboratory of Mechanical Transmission, Chongqing University, Chongqing 400044, China; 20160702066@cqu.edu.cn (F.Z.); xhchen@cqu.edu.cn (X.C.); sunyuanxi@cqu.edu.cn (Y.S.)

² Xi'an Institute of Applied Optics, Xi'an 710065, China; PG29146111@e.ntu.edu.sg

* Correspondence: bailong@cqu.edu.cn

Received: 3 December 2018; Accepted: 18 December 2018; Published: 20 December 2018



Abstract: This paper proposes the design and performance evaluation of a miniaturized continuous hopping robot RHop for unstructured terrain. The hopping mechanism of RHop is realized by an optimized geared symmetric closed-chain multi-bar mechanism that is transformed from the eight-bar mechanism, and the actuator of RHop is realized by a servo motor and the clockwork spring, thereby enabling RHop to realize continuous hopping while its motor rotates continuously only in one direction. Comparative simulations and experiments are conducted for RHop. The results show that RHop can realize better continuous hopping performance, as well as the improvement of energy conversion efficiency from 70.98% to 76.29% when the clockwork spring is applied in the actuator. In addition, comparisons with some state-of-the-art hopping robots are conducted, and the normalized results show that RHop has a better energy storage speed.

Keywords: mobile robot; jumping robot; hopping robot; continuous hopping; single actuator

1. Introduction

With the development of science and technology, robots have become indispensable automation equipment in human society by assisting or replacing humans in various situations. Among mobile robots, hopping robots show a stronger ability to overcome obstacles in the fields of planetary surface exploration, unstructured terrain search, etc. [1–4] when compared with wheeled robots [5], legged robots [6], and tracked robots [7]. The hopping robot was first proposed by Oberth and Seifert [8] in 1967. Then the one-leg jumping model proposed by Raibert [9] became the theoretical research basis for later single-leg jumping robots. As time goes, the NASA three-generation hopping robot [10] and the MIT MICROBOTS [11] significantly progressed the hopping robot research.

According to hopping characteristics of the hopping robot, hopping robots can be classified into two categories: continuous hopping robot and intermittent hopping robot. A continuous hopping robot can recharge its hopping energy in the flying/landing phase, and immediately hop again after contacting the ground, while the intermittent hopping robot needs to realize its energy recharge and hopping attitude adjustment in another ground phase. Currently, continuous hopping robots usually adopt hydraulic [12,13] and pneumatic [14] actuators to realize continuous actuation, which can enable the continuous hopping robot to have high power density and fast drive-response. However, it is still difficult to realize miniaturization and multi-drive coordinated control for them. The intermittent hopping robots usually use their motor as their actuator and use springs as an elastic components [15,16]. Then, by slowly recharging and locking the energy of elastic components by the motor and the hopping mechanism, the intermittent hopping robot can realize hopping once the elastic energy is

released. Due to the limitation of the motor and the complexity of additional energy locking and releasing mechanism in the intermittent hopping robot [15–17], the preparation time that is required to complete a hop will become relatively longer than continuous hopping robots.

The energy locking and releasing mechanism of the hopping robot can be divided into two categories:

- (1) Take advantage of the characteristics of the actuator, either by increasing the number of actuators or by using the forward and reverse rotation of the actuator. For instance, NASA's second-generation frog-inspired hopping robot uses an additionally actuated latching mechanism [10], while the NPU kangaroo-inspired hopping robot additionally uses an actuated ratchet–pawl mechanism [15,16] to realize energy locking and releasing. In addition, the locust-inspired hopping robot designed by Zaitsev et al. [18] and the integrated jumping–crawling robot designed by Jung et al. [17] realizes energy release by reversing the actuating motor. The energy storage and release of these aforementioned robots are all distributed; therefore, it is difficult to absorb the landing impact energy for the next hop.
- (2) Using special devices and irregular component contours such as eccentric cam [19–21], incomplete gear [22–27], etc. to achieve the conversion between energy storage and release. For example, a miniature jumping robot proposed by Zhao et al. [28] uses a quick release detent ball mechanism to hold the spring, and it uses the lever as a strike mechanism to strike the push shaft to release the stored energy. Faraji et al. used two eyebolts located at opposite ends of the rear leg and the fishing line to hold energy for the spider-inspired hopping robot [29], which can release the energy stored in the spring by cut the fishing line. In addition, quadruped robot with jumping ability uses the ratchet and pawl [30], while the first-generation MSU Jumper [31] and the second-generation micro-robots uses one-way bearings. Moreover, the cylinder-shaped robot [32] uses the latch and the hook to realize the conversion of energy state.

Therefore, existing electrically actuated hopping robots have the following disadvantages:

- (1) Increasing the number of actuators in the hopping robot may result in an increase in robot weight as well as the control difficulty. In the meantime, high-intensity forward and reverse rotation of the motor will reduce the electric energy efficiency of the robot, due to energy loss caused by the moment of inertia of the transmission system.
- (2) The design of the special devices increases the difficulty of robot control and reduces the reaction speed of the hopping robot.
- (3) Hopping robots use irregular contours may also suffer from reduced machining accuracy and the wear problem of the contour. The parameters of the incomplete gear and the trajectory of the cam contour, the movement tracks of the hopping mechanism and the limit position of the spring deformation are all required complex coupling design calculations.

Therefore, in this paper, we aim to design a fast-response continuous hopping robot with a single low-power motor that rotates unidirectionally, and the energy storage and release should be simple and reliable without an additional locking and releasing mechanism. (1) Using mechanical evolution, we realize the design of the hopping mechanism while retaining the advantages of the pure linkage mechanism, using the method of 'higher pairs replacing lower pairs' and isomeric mechanisms with same kinematics to meet design objectives. Furthermore, taking into account the transformation characteristics of the compound closed-chain multi-bar mechanism, a symmetrical double-gear-pair 10-bar based continuous hopping robot (named RHop) is proposed (the robotic prototype is shown in Figure 1). (2) Using the characteristics of the periodic motion and the acceleration characteristics during the collinearity of the crank–rocker mechanism, rapid energy storage and release are achieved by the continuous unidirectional rotation of the motor. (3) A clockwork spring is added to the actuation design to amplify the torque of the motor as well as to absorb the landing impact, thereby enabling its continuous and steady hopping.

The rest of this paper is organized as follows: Section 2 introduced the structural design of the RHop; Section 3 proposed the structural optimization and the actuation design; Section 4 performed the prototype experiment and discussion, and Section 5 concluded the paper.



Figure 1. Prototype of the RHop.

2. Structural Design

2.1. Hopping Mechanism Design

Based on the design goals specified in Section 1, the design of the hopping mechanism will be carried out using the method of ‘higher pairs replacing lower pairs’ and isomeric mechanisms with the same kinematics. The preliminary design used pure linkage mechanisms to retain the advantages of the traditional mechanism, and the new mechanism was evolved to meet design objectives when the pure linkage mechanism was unable to meet demand. Finally, the mechanism was improved in series to meet the design goals better.

2.1.1. Design Objectives

To meet the requirements of continuous hopping with fast response, simple and reliable energy storage/release, the first research objectives of this paper is established as:

- (1) Using only one motor that is as small as possible.
- (2) The motor should only rotate unidirectionally.

Due to the inherent characteristic in kinematics of the hopping mechanism, it will add unnecessary angular momentum to the robot system if there is a horizontal component of ground reaction force (GRF) in the direction of take-off, thereby endangering the stability of hopping posture. For example, the direction of the GRF should be close to the vertical direction when the robot’s take-off angle is 90° . Based on this requirement, the second research objective of this paper is proposed as: achieving non-rotation or minimal rotation of the robot (sagittal plane) to take-off, which means the robot take-off with near-zero angular velocity and the system has no additional angular momentum. To materialize this requirement, we present the following two design objectives:

- (3) The foot trajectory curve of the hopping mechanism should (a) be a straight line; (b) pass through the center of mass (CM) of the robot; (c) be consistent with the take-off direction of the hopping robot.
- (4) Minimize the moment acting on the robot’s CM when the robot component moves.

At the same time, for the miniaturization of the robot, the following design objectives are proposed:

- (5) The foot trajectory curve of the hopping mechanism should be located within its mechanism.
- (6) The structure of the hopping mechanism is compact.

2.1.2. Preliminary Configuration

In order to design the configuration of the hopping mechanism by evolving the closed-chain multi-bar isomeric mechanisms with same kinematics, as well as satisfying the aforementioned design requirements (DR.), the degree of freedom (DOF) of the planar mechanism is first studied.

The equation for calculating the DOF of a planar mechanism is:

$$F = 3n - 2p_L - p_H \tag{1}$$

where N represents the number of components in the planar mechanism, where $n = N - 1$ is the number of moving components, p_L is the number of lower pairs and p_H is the number of higher pairs.

To satisfy DR.1, the DOF of the robot needs to be set to one. When using the pure linkage mechanism to design the hopping mechanism, the number of higher pairs ($p_H = 0$) can be omitted, i.e.,

$$F = 3n - 2p_L = 1 \tag{2}$$

Table 1 lists the desirable permutations of Equation (2).

Table 1. The desirable permutations of Equation (2).

Config.	config.1	config.2	config.3	config.4	config.5	...
n	1	3	5	7	9	...
p_L	1	4	7	10	13	...

Config.1 does not exist; config.2 is a common single closed-chain four-bar mechanism; config.3 is a closed-chain six-bar linkage (Watt type and Stephenson type), as shown in Figure 2. Config.4 is a closed-chain eight-bar linkage, in which 16 main configurations of kinematical chain are shown in Figure 3 [33]. Config.5 is a closed-chain 10-bar linkage, which includes 230 specific configurations [34].

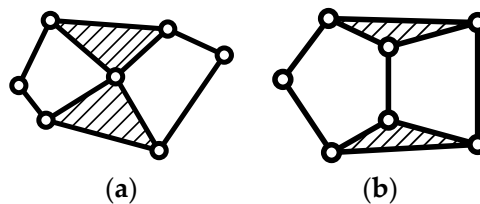


Figure 2. Kinematical chain of the closed-chain six-bar mechanism with a single degree of freedom (DOF). (a) Watt type. (b) Stephenson type.

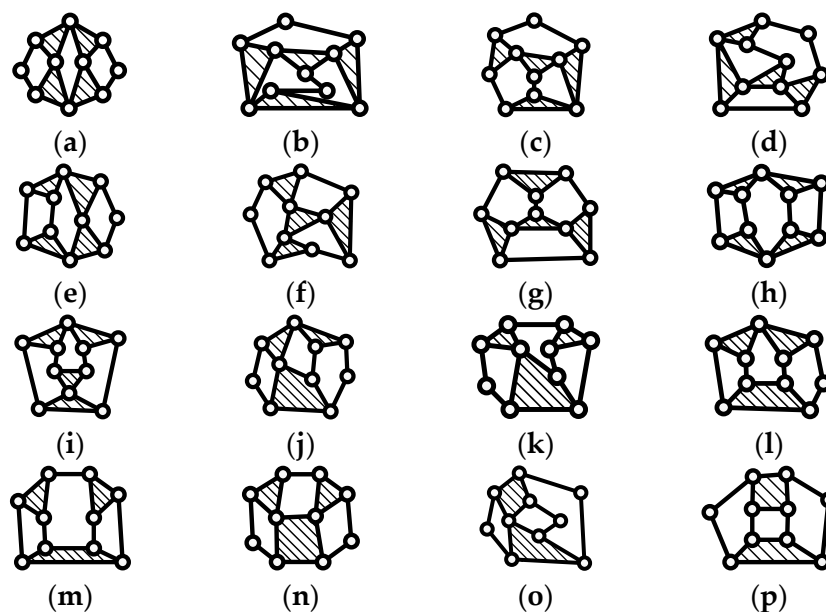


Figure 3. Kinematical chain of closed-chain eight-bar mechanism with a single DOF.

The four-bar mechanism is difficult to meet the requirements of complex motion performance and rich trajectory due to its few optimization parameters. The configuration of the 10-bar linkage is too complicated and changeable. Therefore, the single DOF six-bar linkage and eight-bar linkage are preselected for the mechanical design of RHop.

DR.4 requires that the horizontal acceleration of the CM caused by the inertia of the moving component needs to be eliminated. Therefore, the bilateral symmetric kinematical chain configuration is chosen as the basic structural configuration of the hopping robot. Watt and Stephenson types of the six-bar linkage and the type (a), (b), (e), (f), (g), (h), (i), (m), (n), (o), and (p) of the eight-bar linkage shown in Figure 3 can all meet this requirement. According to the drive mode indicated in DR.2, the input bar needs the function of circumferential rotation to form the crank-rocker mechanism. The kinematical chain configurations in the eight-bar linkage satisfy the condition are (m), (n), and (p), and the six-bar linkage does not satisfy the condition of existing the crank-rocker mechanism.

2.1.3. Configuration Adjustment

To use a common rotary motor as the power source, the two cranks need to rotate at the same speed with an opposite direction. Therefore, the gear pair with a confirmed transmission ratio is introduced into the eight-bar mechanism. Since the revolute pairs in the desired eight-bar mechanism are all lower pairs, it is necessary to perform 'higher pairs replacing lower pairs' to convert the two cranks and the related bars into a pair of geared crank-rocker mechanisms.

Any planar mechanism with lower pairs can be considered as consisting of several connected Assur groups [35]. To find a suitable mechanism, in which revolute pairs can be successfully replaced by gear pairs [36,37], attempts of transforming configuration (m), (p), and (n) via Assur groups are depicted in Figure 4.

As can be obtained from Figure 4, only the configurations (n) can be totally transformed, in which the crank mechanism consists of the bar 4 and 6.

2.1.4. Structural Improvement

P_7 and P_8 (Figure 4c) in the bilateral symmetric gear-crank-rocker mechanism are set as the output. The motion trajectories of points P_7 and P_8 are circular arcs with points P_5 and P_6 as their arc center, respectively. However, this output trajectory cannot meet DR.3. Therefore, additional motion components should be added to meet the required foot motion trajectory. Since the required hopping mechanism in this paper is a bilateral symmetric mechanism, and it does not contradict with DR.1 and DR.4, then the additional number of moving components n' , the number of lower pairs p'_L and the number of higher pairs p'_H must satisfy the following Equation (3):

$$3n' = 2p'_L + p'_H \quad (3)$$

After full investigation of common mechanism, the gear-linkage mechanism was finally selected as the additional moving component for the hopping mechanism. To ensure that the structure of the hopping mechanism is compact without changing its symmetry properties, a symmetrical gear-linkage mechanism with the least number of components, that is, the symmetrical gear-three-bars mechanism shown in Figure 4d, was selected. The output bars P_5P_7 and P_6P_8 were extended to bars with three revolute pairs, the newly added revolute pairs in which are articulated to the non-gear ends of the symmetrical gear-three-bar mechanism. Therefore, the whole bilateral symmetric gear-crank-rocker mechanism finally evolved into a symmetrical double-gear-pair ten-bar mechanism with a single DOF, as shown in Figure 4d, which was consistent with DR.1 to DR.4.

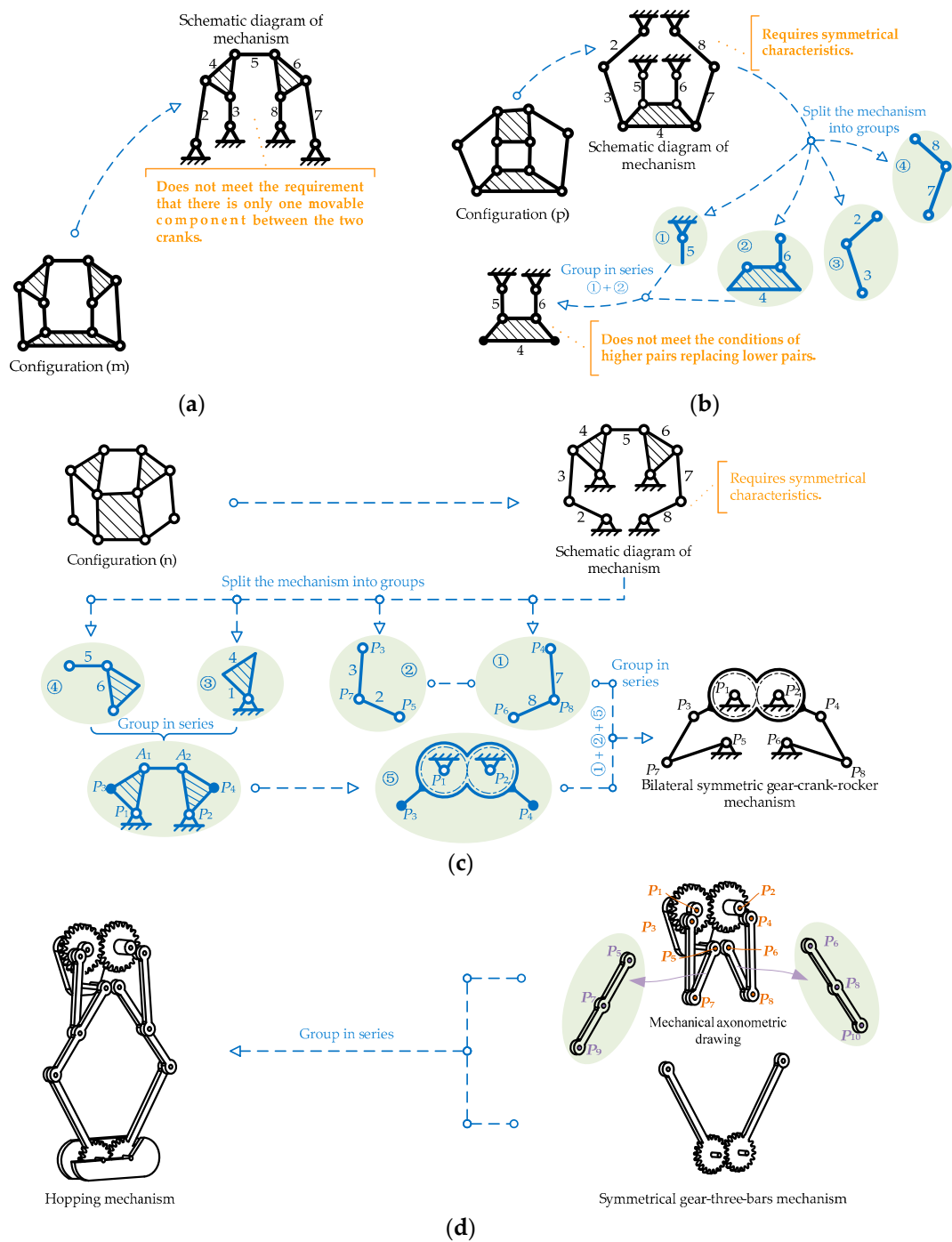


Figure 4. Configuration evolution of the eight-bar mechanism. (a) The evolution of the configuration (m). (b) The evolution of the configuration (p). (c) The evolution of the configuration (n). (d) The process of structural improvement.

2.2. Energy Mechanism Design

The energy mechanism should be designed to realize the storage/release of elastic energy for hopping. Most existing electrically actuated hopping robots use springs as the energy storage/release elements, which have the advantages of small mass and high controllability. Therefore, in this paper, we will utilize the tension spring to design the energy mechanism for the RHop.

When a crank works as the driving linkage, the rocker will be the driven linkage with a reciprocating swing in variable speed. The crank will have two chances of being collinear, with the connecting rods

in one locomotion cycle. When the crank and the connecting rod are collinear for the second time, the swing speed of the rod will reach its tipping point, i.e., its acceleration will reach the largest. Based on these characteristics, we finally placed the tension spring between two points P_9 and P_{10} , as shown in Figure 5. This design has the following benefits:

Assume that crank P_1P_3 is the active component that rotates one turn in one motion cycle, and that the horizontal axis represents the rotation angle α of the crank.

- (1) When the rotation angle is $\alpha_1 = 0$, the crank and the connecting rods will be collinear for the first time. This will be the crucial moment where the distance between points P_9 and P_{10} is the smallest. This also will be the initial position of the energy storage phase, as shown in Figure 5a.
- (2) Within the range of $\alpha_1-\alpha_2$, the distance between P_9 and P_{10} will gradually increase, and the length of the spring will gradually grow.
- (3) When the rotation angle reaches α_3 , the crank and the connecting rods are collinear for the second time. At this time, the distance between point P_9 and P_{10} will be the largest, which will be the end position of the energy storage phase, as shown in Figure 5c. It can also be noticed that the feature of the crank-rocker mechanism is properly compatible with the required hopping burst characteristics.
- (4) Within the range of $\alpha_3-\alpha_4$, the distance between the point P_9 and P_{10} will gradually decrease. Figure 5d shows the general position of this energy release phase.
- (5) When the rotation angle is $\alpha_5 = 360^\circ$, the mechanism will return to its initial position of the energy storage phase, thus preparing for the next hopping cycle.

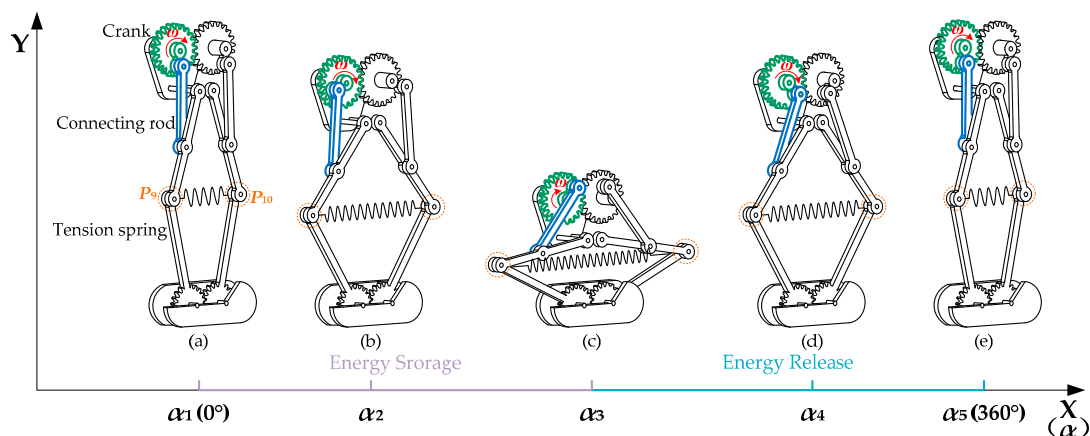


Figure 5. The energy storage and release phases. α in the horizontal axis represents the rotation angle of the crank. (a) The initial position of the energy storage phase, which means that the tension spring is in a natural state. (b) The general position of the energy storage phase. (c) The end position of the energy storage phase, which means that the energy storage of the tension spring is maximum. (d) The general position of the energy release phase. (e) The initial position of the energy storage phase.

3. Structural Optimization and Actuation Design

3.1. Structural Optimization

3.1.1. Kinematics Analysis

According to the selected configuration of the hopping mechanism in Figure 4d, the kinematics model of the hopping mechanism is depicted in Figure 6. Because the selected configuration of the hopping mechanism is symmetrical (the branched chain $P_2-P_4-P_8-P_{10}-P_{12}-P_6$ is symmetric with the branched chain $P_1-P_3-P_7-P_9-P_{11}-P_5$), and only one of the branched chains is selected for kinematic analysis (the branched chain $P_2-P_4-P_8-P_{10}-P_{12}-P_6$ is selected).

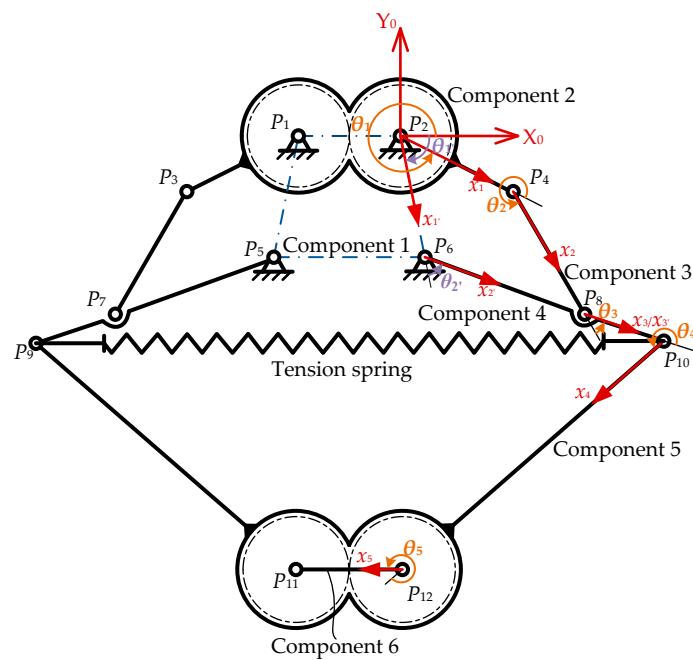


Figure 6. The kinematics model of the hopping mechanism. Where component 1 is the frame $P_1P_5P_6P_2$; component 2 is the crank–gear–bar P_2P_4 ; component 3 is the connecting rod P_4P_8 ; component 4 is the rocker $P_6P_8P_{10}$; component 5 is the gear–bar $P_{10}P_{12}$; component 6 is the connecting rod $P_{12}P_{11}$ that is connected with the rotation center of the gear–bar.

According to the Denavit–Hartenberg Method [38], the homogeneous transformation matrix from the $i-1$ coordinate system to the i coordinate system is:

$${}^{i-1}T_i = \begin{bmatrix} C\theta_i & -S\theta_i & 0 & a_{i-1} \\ C\alpha_{i-1}S\theta_i & C\alpha_{i-1}C\theta_i & -S\alpha_{i-1} & -d_iS\alpha_{i-1} \\ S\alpha_{i-1}S\theta_i & S\alpha_{i-1}C\theta_i & C\alpha_{i-1} & d_iC\alpha_{i-1} \\ 0 & 0 & 0 & 1 \end{bmatrix} \quad (4)$$

where $C\theta_i \triangleq C(\theta_i) \triangleq \cos(\theta_i)$, $S\theta_i \triangleq S(\theta_i) \triangleq \sin(\theta_i)$.

In Figure 6, the branched chain $P_2-P_4-P_8-P_{10}-P_{12}-P_6$ can be further subdivided into two branched chains, the main chain $P_2-P_4-P_8-P_{10}-P_{12}$ and the secondary chain $P_2-P_6-P_8-P_{10}$. The specific D-H parameters of the main and secondary chain are shown in Table A1 in Appendix A.

According to Table A1 and Equation (4), the position vectors of each hinge in the main chain and the secondary chain in the fixed coordinate system are:

$$\begin{cases} r_{P_4}^T = l_{P_2P_4} \begin{bmatrix} C\theta_1 & S\theta_1 & 0 \end{bmatrix} \\ r_{P_8}^T = r_{P_4}^T + l_{P_4P_8} \begin{bmatrix} C(\theta_{1+2}) & S(\theta_{1+2}) & 0 \end{bmatrix} \\ r_{P_{10}}^T = r_{P_8}^T + l_{P_8P_{10}} \begin{bmatrix} C(\theta_{1+2+3}) & S(\theta_{1+2+3}) & 0 \end{bmatrix} \\ r_{P_{12}}^T = r_{P_{10}}^T + l_{P_{10}P_{12}} \begin{bmatrix} C(\theta_{1+2+3+4}) & S(\theta_{1+2+3+4}) & 0 \end{bmatrix} \\ r'_{P_6}{}^T = l_{P_2P_6} \begin{bmatrix} C\theta_{1'} & -S\theta_{1'} & 0 \end{bmatrix} \\ r'_{P_8}{}^T = r'_{P_6}{}^T + l_{P_6P_8} \begin{bmatrix} C(\theta_{1'-2'}) & -S(\theta_{1'-2'}) & 0 \end{bmatrix} \end{cases} \quad (5)$$

where r_A is the position vector of the hinge A in the main chain; $r_A = [A_x \ A_y \ A_z]^T$; r'_A is the position vector of the hinge A in the secondary chain; $r'_A = [A'_x \ A'_y \ A'_z]^T$; $\theta_{i+j} = \theta_i + \theta_j$, $\theta_{i-j} = \theta_i - \theta_j$.

The hopping mechanism has the characteristics of symmetry and is combined with Equation (5); the expression for the position vector of each joint point in the branched chain $P_1-P_3-P_7-P_9-P_{11}-P_5$ is:

$$\begin{cases} r_{P_3}^T = \begin{bmatrix} -P_{4x} - CL & P_{4y} & 0 \end{bmatrix} \\ r_{P_7}^T = \begin{bmatrix} -P_{8x} - CL & P_{8y} & 0 \end{bmatrix} \\ r_{P_9}^T = \begin{bmatrix} -P_{10x} - CL & P_{10y} & 0 \end{bmatrix} \\ r_{P_{11}}^T = \begin{bmatrix} -P_{12x} - CL & P_{12y} & 0 \end{bmatrix} \\ r'_{P_5}^T = \begin{bmatrix} -P_{6x'} - CL & P_{6y'} & 0 \end{bmatrix} \end{cases} \quad (6)$$

where $CL = l_{P_1 P_2}$.

3.1.2. Establishment of Optimization

It is important and necessary to optimize the dimension of the closed-chain mechanism [39]. Because of the dual-objective optimization, the special method of TOPSIS (Technique for Order Preference by Similarity to an Ideal Solution) was chosen for dimension optimization. The same trend of evaluation indicators facilitates a reasonable compromise between the two optimization objectives. Initially proposed by Hwang and Yoon in 1981 [40–42], two vectors are constructed:

$$F^* = [f_m^*, f_n^*]^T \quad (7)$$

$$F(\mathbf{X}) = [f_m(\mathbf{X}), f_n(\mathbf{X})]^T \quad (8)$$

The vector represented by Equation (7) is regarded as an ideal point of the vector function represented by Equation (8). Then the smaller the deviation between $F(\mathbf{X})$ and F^* , the closer the objective function will be to the ideal point, i.e., the closer the design variable will be to the optimal solution.

The distance equation of the TOPSIS Method is:

$$F_d = \|F(\mathbf{X}) - F^*\| = \left\{ \sum_{i=1}^n \lambda_j [f_j(x_i) - f_j^*]^p \right\}^{\frac{1}{p}} \quad (9)$$

where $p \in [1, +\infty)$. When $p = 1$, it is the Hamming distance or absolute distance; when $p = 2$, it is the Euclidean distance; when $p = \infty$, it is the Chebyshev distance. In this paper, $p = 2$ was selected due to the optimization function dimension and distance characteristics.

(1) Objective function

First, to maximize the energy that is stored in the hopping mechanism, the tension spring is required to have the greatest amount of tensile deformation. Second, to make the structure more compact, the minimum longitudinal dimension of the mechanism is also required. Assuming that the sampling position in one hopping cycle is n , then the dual-objective optimization objective function can be expressed as:

$$\begin{cases} f_1(\mathbf{X}) = \min \left[\min_{i=1}^n (P_{10x_i} - P_{9x_i}) - \max_{i=1}^n (P_{10x_i} - P_{9x_i}) \right] \\ f_2(\mathbf{X}) = \min \left[\max_{i=1}^n (P_{2y_i} - P_{12y_i}) \right] \end{cases} \quad (10)$$

where \mathbf{X} represents the design variable matrix; P_{10x_i} is the horizontal position of P_{10} at the i th sampling position; P_{9x_i} is the horizontal position of P_9 at the i th sampling position; P_{2y_i} is the vertical position of P_2 at the i th sampling position; P_{12y_i} is the vertical position of P_{12} at the i th sampling position.

(2) Design variables

It can be seen from Equation (10) that the optimization objective is related to the coordinates of points P_9 , P_{10} , and P_{12} . As can be also noticed from Section 3.1.1, the coordinates of these three points

are determined by (1) the length of each linkage, (2) the angle between the line connecting the hinge points P_2 & P_6 and the X_0 -axis direction, and (3) the position of the crank–gear–bar. Therefore, the optimization variables matrix \mathbf{X} can be concluded as being:

$$\mathbf{X} = [x_1, x_2, x_3, x_4, x_5, x_6, x_7, x_8, x_9, x_{10}]^T = [l_1, l_2, l_3, l_4, l_5, l_6, l_7, l_8, \beta_1, \beta_2]^T \tag{11}$$

where $l_1 = l_{P_1P_2}$; $l_2 = l_{P_2P_4}$; $l_3 = l_{P_2P_6}$; $l_4 = l_{P_6P_8}$; $l_5 = l_{P_4P_8}$; $l_6 = l_{P_8P_{10}}$; $l_7 = l_{P_{10}P_{12}}$; $l_8 = l_{P_{12}P_{11}}$; $\beta_2 = \theta_1'$. β_1 is the angle between the initial position of the crank–gear–bar P_2P_4 and the positive direction of the X_0 -axis.

(3) Constraint conditions

According to the conditions for the existence of a crank–rocker mechanism in the planar four-bar linkage $P_2P_4P_8P_6$, the bars l_2, l_3, l_4 , and l_5 have the following linear constraints:

$$A_1\mathbf{X} \leq \mathbf{b}_1 \tag{12}$$

Considering the limitation of the processing technology of the component and the requirement for the non-interference of installation position, the linear constraints of geometric dimensions are given as:

$$A_2\mathbf{X} \leq \mathbf{b}_2 \tag{13}$$

According to the requirements of the overall size of the robot, design variables should be restrained, that is:

$$\begin{cases} \mathbf{X} \geq \mathbf{d}_{min} \\ \mathbf{X} \leq \mathbf{d}_{max} \end{cases} \tag{14}$$

Based on the actual processing requirements of the frame, the limitations of the original length and tensile deformation of the tension spring, the following nonlinear constraints exist:

$$\Phi(\mathbf{X}) \leq \mathbf{G} \tag{15}$$

The main chain and the secondary chain are coupled at the joint P_8 . The slopes of the link P_6P_8 and P_8P_{10} are equal. This is because the relative distance between point P_{11} and P_{12} along the X_0 -axis is constant, i.e., there is a constraint relationship $P_{12x} - P_{11x} = l_8$. Therefore, the closed-chain vector constraint of the hopping mechanism given is:

$$H(\mathbf{X}) = 0 \tag{16}$$

The specific process of establishing the constraint conditions of the optimization model is detailed in Appendix A.

(4) Optimization Model

According to Equation (7)–(16), the dimension optimization mathematical model of the robot hopping mechanism can be obtained as follows:

$$\begin{cases} \mathbf{X} = [x_1, x_2, \dots, x_{10}]^T \\ \min f_1(\mathbf{X}); f_2(\mathbf{X}) \\ s.t. \quad A_1\mathbf{X} \leq \mathbf{b}_1; \quad A_2\mathbf{X} \leq \mathbf{b}_2 \\ \quad \quad \mathbf{X} \leq \mathbf{d}_{max}; \quad \mathbf{X} \geq \mathbf{d}_{min} \\ \quad \quad \Phi(\mathbf{X}) \leq \mathbf{G}; \quad H(\mathbf{X}) = 0 \end{cases} \tag{17}$$

3.1.3. Optimization Process and Results

The flow chart of the optimization process is shown in Figure 7. The program is implemented in Matlab, and the optimization results are listed in Table 2.

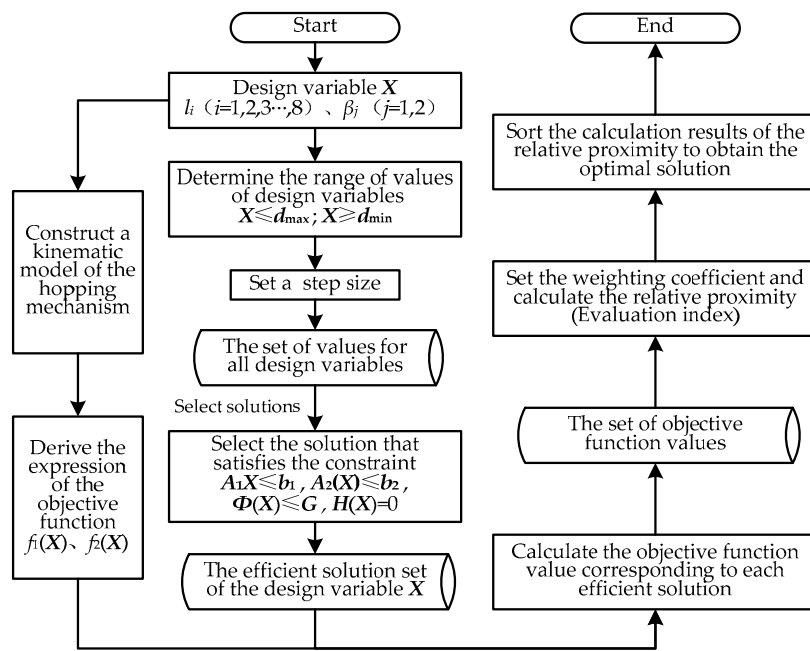


Figure 7. The flow chart of the optimization.

Table 2. Optimization results of the hopping mechanism dimensions.

Optimization Parameters	l_1/mm	l_2/mm	l_3/mm	l_4/mm	l_5/mm
Optimization Results	30.000	15.729	32.000	50.939	52.851
Optimization Parameters	l_6/mm	l_7/mm	l_8/mm	$\beta_1/(\text{°})$	$\beta_2/(\text{°})$
Optimization Results	34.061	75.000	25.000	276.180°	134.768°

By analyzing the data shown in Table 2, it can be proven that: (1) The optimization result satisfies the range of values of the design variables; (2) The bars $l_2, l_3, l_4,$ and l_5 satisfy the constraints of the crank–rocker mechanism; (3) The dimension of the bars l_1, l_2, l_3 avoid interference during assembly; (4) Optimized data meets the constraints on the kinematical chain. The optimized method is used to gain a set of ideal data.

The graphical optimization result is shown in Figure 8a. To avoid interference during hopping, changes are made to the optimization result, and the solid hopping mechanism model is shown in Figure 8b.

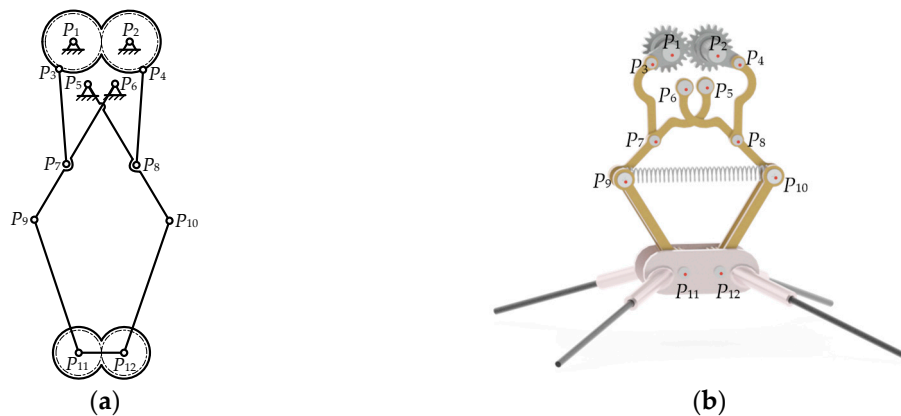


Figure 8. Hopping mechanism. (a) Optimization result. (b) Solid model.

3.2. Actuation Design

3.2.1. Theoretical Analysis

The actuator of the hopping robot has the following requirements.

- (1) In the process of energy storage, the actuator needs to provide the crank–gear–bar great driving torque to realize the relative movement between point P_9 and P_{10} , thereby realizing the elongation of the tension spring.
- (2) When the energy is released, the angular velocity of the crank will change dramatically within a very short period. Therefore, it is necessary to reduce the resistance from the motor.
- (3) When the hopping robot lands, it is necessary to absorb the landing shock to reduce the damage to the motor.

Therefore, a clockwork spring that is capable of storing and releasing angular energy is introduced between the output shaft of the motor and the crank–gear–bar as an auxiliary energy storage element, as shown in Figure 9. There are three advantages of the proposed special actuator.

- (1) The input torque of the drive motor is amplified by the clockwork spring, thereby reducing the requirement for the motor output power. At the same time, the great torque provided by the actuator can be released in a very short time.
- (2) The great torque releasing speed mentioned in (1) can drive the crank–gear–bar to cross the limit position of the hopping mechanism quickly, thereby realizing the explosive hop of the robot.
- (3) The clockwork spring also absorbs the impact of hopping on the motor.

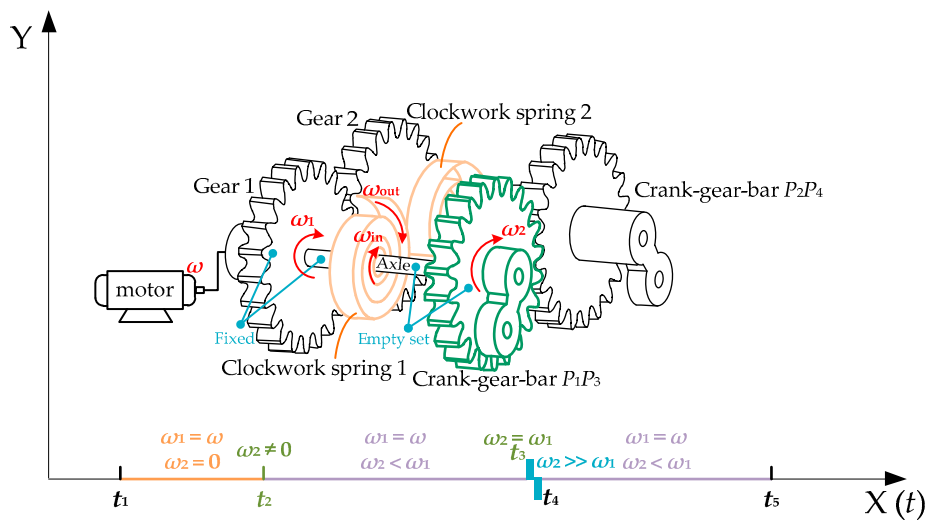


Figure 9. Energy-stored type actuator. The clockwork spring is introduced between the motor output shaft and the crank–gear–bar as an auxiliary energy storage element.

The crank–gear–bar P_1P_3 and P_2P_4 are an empty set in the shaft, the gear 1 and the gear 2 are fixed at the other end of the two shafts respectively, and mesh with each other. Gear 1 is driven by the motor, and the inner ring of the clockwork spring 1 and 2 are fixed on gear 1 and 2 respectively, which means $\omega_{in} = \omega_1$. The outer rings are fixed on crank–gear–bar P_1P_3 and P_2P_4 respectively, which means $\omega_{out} = \omega_2$. When the motor continuously rotates in the clockwise direction, the angular velocity of the motor is ω . The relationship between the actuator and the active component is shown in Figure 9.

- (1) During the period t_1-t_2 , $\omega_1 = \omega$ and $\omega_2 = 0$. At this phase, the inner and outer ring of the clockwork spring generates a difference in speed, and the clockwork spring begins to store energy.

- (2) At the moment t_2 , the angular velocity of the crank–gear–bar changes, i.e., $\omega_2 \neq 0$. During the period $t_2 - t_3$, $\omega_2 \neq 0$ but $\omega_2 < \omega_1$. There is still a difference in the speed between the inner and outer rings of the clockwork spring, which means that the spring can still store energy, but the energy storage speed slows down.
- (3) At the moment t_3 , the clockwork spring rotates to its limit position, the angular velocity is $\omega_2 = \omega_1$. The inner and outer rings of the clockwork spring rotate at the same speed, which means that the process of energy storage of the clockwork spring is over.
- (4) In a very short time from $t_3 - t_4$, the energy stored in the clockwork spring is released, and the angular velocity is $\omega_2 \gg \omega_1$.
- (5) During the period $t_4 - t_5$, the angular velocity is $\omega_2 < \omega_1$. When the time reaches t_4 , the next hopping cycle begins.

3.2.2. Actuator Verification

To explore the influence of the clockwork spring on the hopping performance of the robot, as well as the above theoretical analysis, dynamics simulations were performed for the hopping robot HR-A (with special actuator) and hopping robot HR-B (only with the rigid motor).

Figure 10 shows the deformation velocity of the tension spring and the angular velocity of the crank–gear–bar P_1P_3 of the HR-A. The X-axis is the simulation time. The blue dashed line represents the deformation velocity of the tension spring (corresponding to the right Y-axis), and the red solid line represents the angular velocity of the P_1P_3 (corresponding to the left Y-axis).

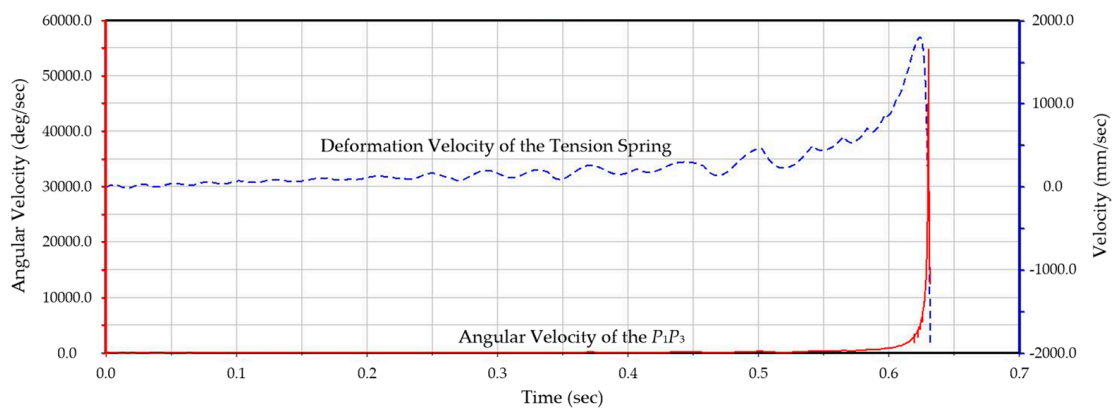


Figure 10. Simulation results of the HR-A. The deformation velocity of the tension spring and the angular velocity of the crank–gear–bar P_1P_3 .

In the early and middle phases of the hopping cycle, the deformation velocity of the tension spring increases slowly as the angular velocity of the crank–gear–bar P_1P_3 grows gradually. However, in the late stage, the deformation velocity of the tension spring and the angular velocity of the crank–gear–bar P_1P_3 both sharply increase, indicating that the effect of the clockwork spring in the actuator is effective in storing elastic energy for hopping.

To further investigate the performance of the proposed actuator, the deformation velocities of the tension springs in HR-A and HR-B are compared, as shown in Figure 11a. Where the blue dashed line represents the deformation velocity of the tension spring in HR-A, and the red solid line represents the deformation velocity of the tension spring in HR-B. For HR-A, the deformation velocity of its tension spring increases slowly before $t = 0.521$ s. After this time, the energy of the clockwork spring is released, then the deformation speed of the tension spring increases rapidly, reducing the energy storage time to 0.63 s. However, the deformation velocity of tension spring in HR-B only grows and decreases steadily in its whole energy storage phase, which reaches the length of 0.704 s. Key positions in the simulation of HR-A and HR-B are compared in Figure 11b.

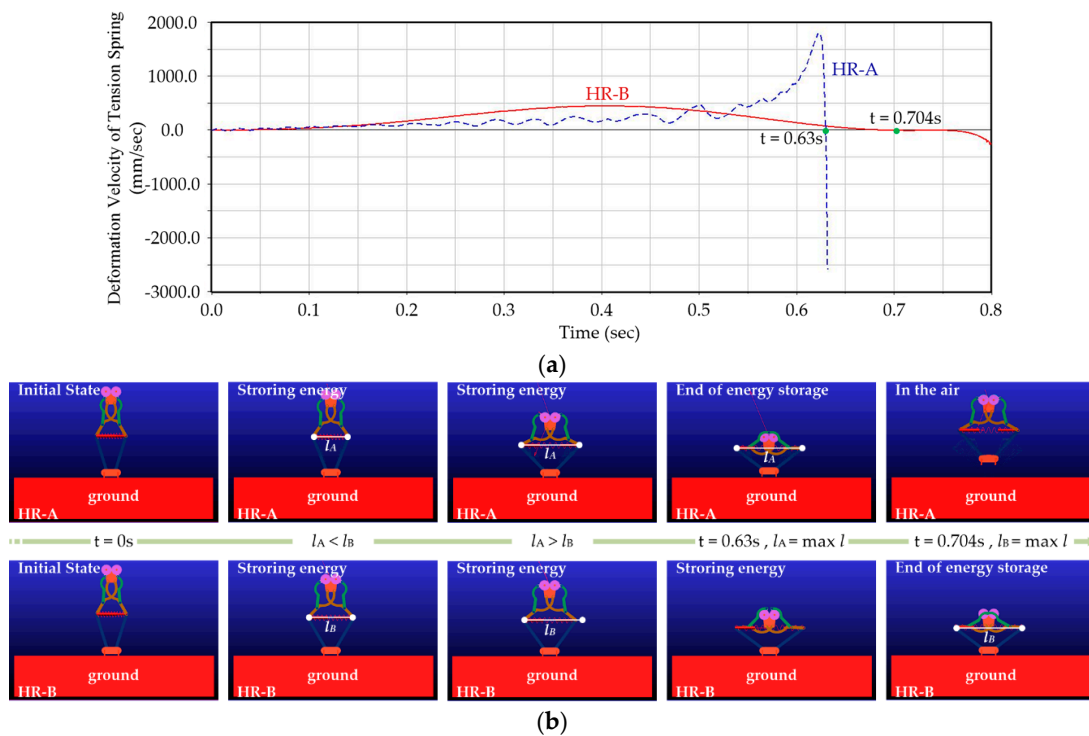


Figure 11. Comparison of simulation results for HR-A and HR-B. (a) The deformation velocity of the tension spring. (b) Key positions in the simulation. l_i means the length of the tension spring.

4. Prototype Implementation and Experiment

4.1. Prototype Design

The prototype of RHop is shown in Figure 12. The main structural parts are manufactured by 3D printing, and the axles are made of carbon fiber rods to reduce the overall weight of the RHop. The driving motor adopts a servo that can rotate around the whole circumference, with an output driving torque of 0.22 N·m. The prototype size is 252 mm × 155 mm × 85 mm, and its weight is about 560 g (including batteries, motor, etc.).

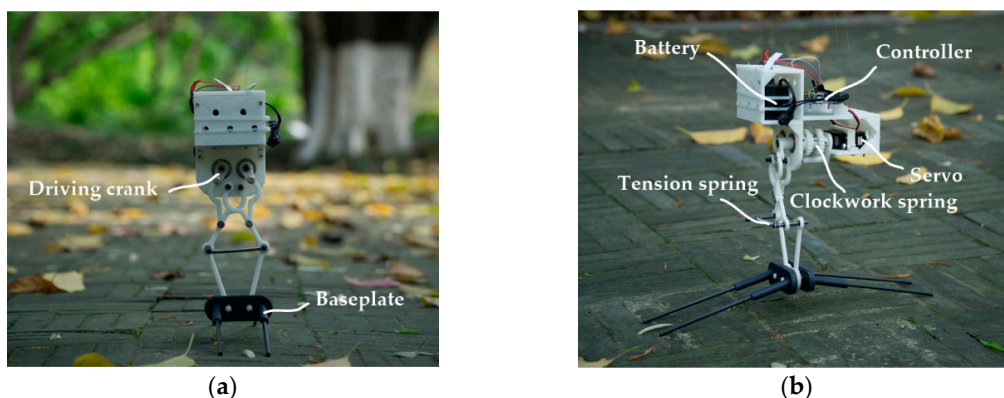


Figure 12. Robotic prototype. (a) Front view. (b) Side view.

4.2. Hopping Performance Analysis

4.2.1. Foot Trajectory Verification

By substituting the optimization results of the hopping mechanism into Equations (5) and (6), the movement posture of the hopping mechanism in the energy storage phase can be obtained, as shown

in Figure 13a. Point A of the connecting link $P_{11}P_{12}$ was selected as the reference point to obtain the foot trajectory curve.

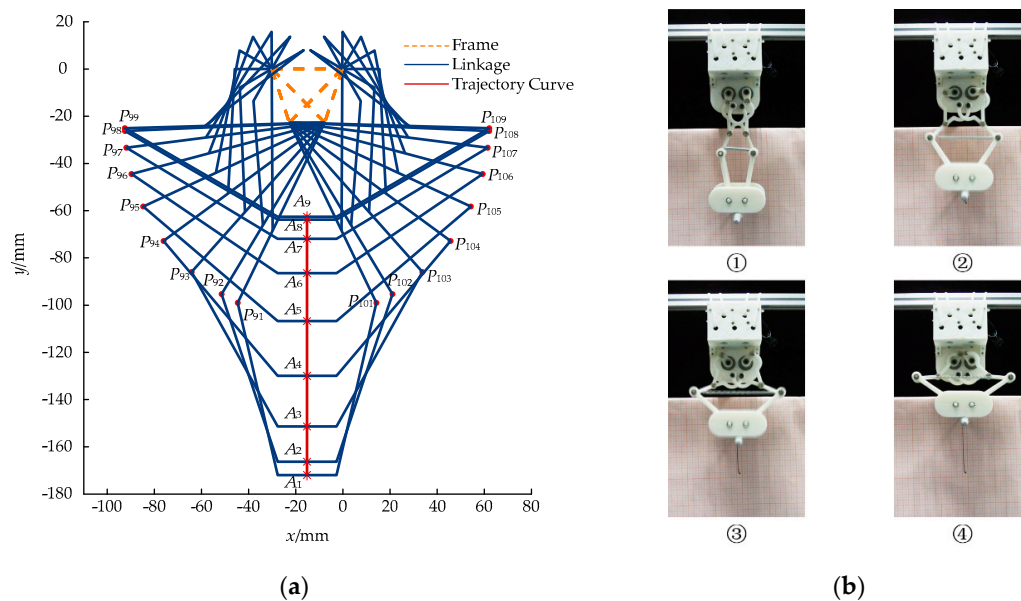


Figure 13. (a) Theoretical movement posture of the hopping mechanism at the energy storage phase. (b) Experimental process diagram of trajectory reproduction at energy storage phase. ① represents the initial position; ② and ③ represents the general position; ④ represents the end position.

As shown in Figure 13a, the theoretical foot trajectory is a straight line perpendicular to the X-axis, and meets the requirements of DR.3–DR.6. In addition, the stretching deformation of the optimized hopping mechanism during the energy storage phase can reach $\Delta l = 96$ mm, which is longer than the height of the whole hopping robot RHop.

To obtain the foot trajectory of the prototype, the body of the hopping robot was fixed. A paint pen was installed at the center of the foot of the robot, thereby enabling the trajectory to be drawn on the scale paper. In the scale paper, the horizontal and vertical distance of each grid was 1 mm. Figure 13b shows the experimental process.

The comparison of the theoretical and the experimental foot trajectories are depicted in Figure 14. Specific comparison results are listed in Table 3.

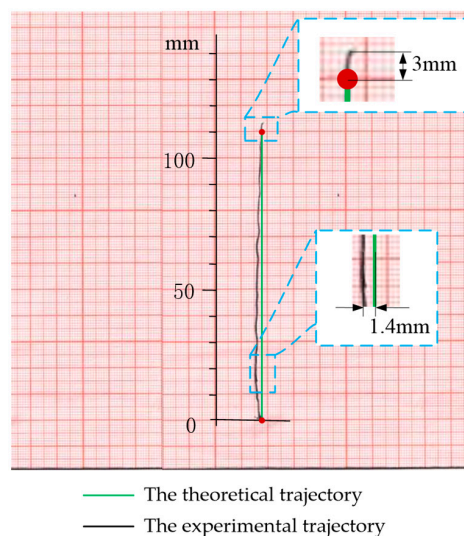


Figure 14. Comparison of the foot trajectory between theory and experiment.

Table 3. Trajectory sampling analysis results.

Horizontal Deviation	Vertical Deviation	Average Deviation	Root Mean Squared Error
1.4 mm	3 mm	0.7345 mm	0.8543 mm

It can be seen that the foot trajectory obtained from the experiment is an approximate straight line perpendicular to the x-axis, which differs by about 3 mm from the theoretical trajectory in the vertical direction, and the maximum horizontal deviation of the trajectory is about 1.4 mm.

The main reasons for the deviation are concluded as follows:

- (1) Insufficient accuracy of 3D printing manufacture, which makes it hard to achieve a completely symmetrical structure during assembly.
- (2) Vibration in the experiment.

4.2.2. Hopping Performance Verification

To verify the correctness of the theory of the mechanism and the actuator design, as well as the feasibility of using a single motor with continuous circumferential rotation in one direction to achieve continuous hop, the prototype was mounted on a vertical slide rail to constrain its lateral deflection for the avoidance of the negative effects of unsteady landing and taking-off in continuous hopping (The video file titled “Experimental Video-RHop.mp4”, which can be found in the Supplementary Materials).

Two prototypes were tested in the experiment, i.e., (a) the prototype equipped with the special actuator, and (b) the prototype, just equipped with a rigid motor.

Tension springs with different stiffness were tested for whether they could achieve energy storage. When the stiffness of the tension spring was less than or equal to 398.3 N/m, both prototypes could achieve the energy storage and hopping. When the stiffness of the tension spring was greater than 455.2 N/m, neither type of prototype could achieve energy storage and hop; When the stiffness was within the range of aforementioned limit values, only the first prototype could achieve the energy storage and hopping. This proves that the robot that equipped with the special actuator could amplify its output torque with the same motor, thereby improving the hopping performance. Figure 15 shows the experimental process of the two prototypes using $k = 398.3$ N/m tension springs. The energy storage time required for the first prototype was 0.871 s, and it could hop up to 129 mm. However, the second prototype needed 1.236 s and could just hop up to 120 mm. Let the ratio γ between the gravitational potential energy at the highest point of the robot E_p and the elastic potential energy of the tension spring E_{ps} be defined as the energy conversion efficiency of the robotic hopping mechanism. Then, the energy equation of two prototype can be measured as $E_{ps} = 1.392$ J, $E_{p1} = 1.062$ J and $E_{p2} = 0.988$ J, i.e., the energy conversion efficiency of the first prototype is $\gamma_1 = 76.29\%$, and the second one is $\gamma_2 = 70.98\%$, which proves that the first prototype can greatly reduce its energy storage time and improves its energy efficiency by 5.31%. The main reasons for the loss of elastic potential energy are the friction at the hinged joint and the friction of the slide rail.

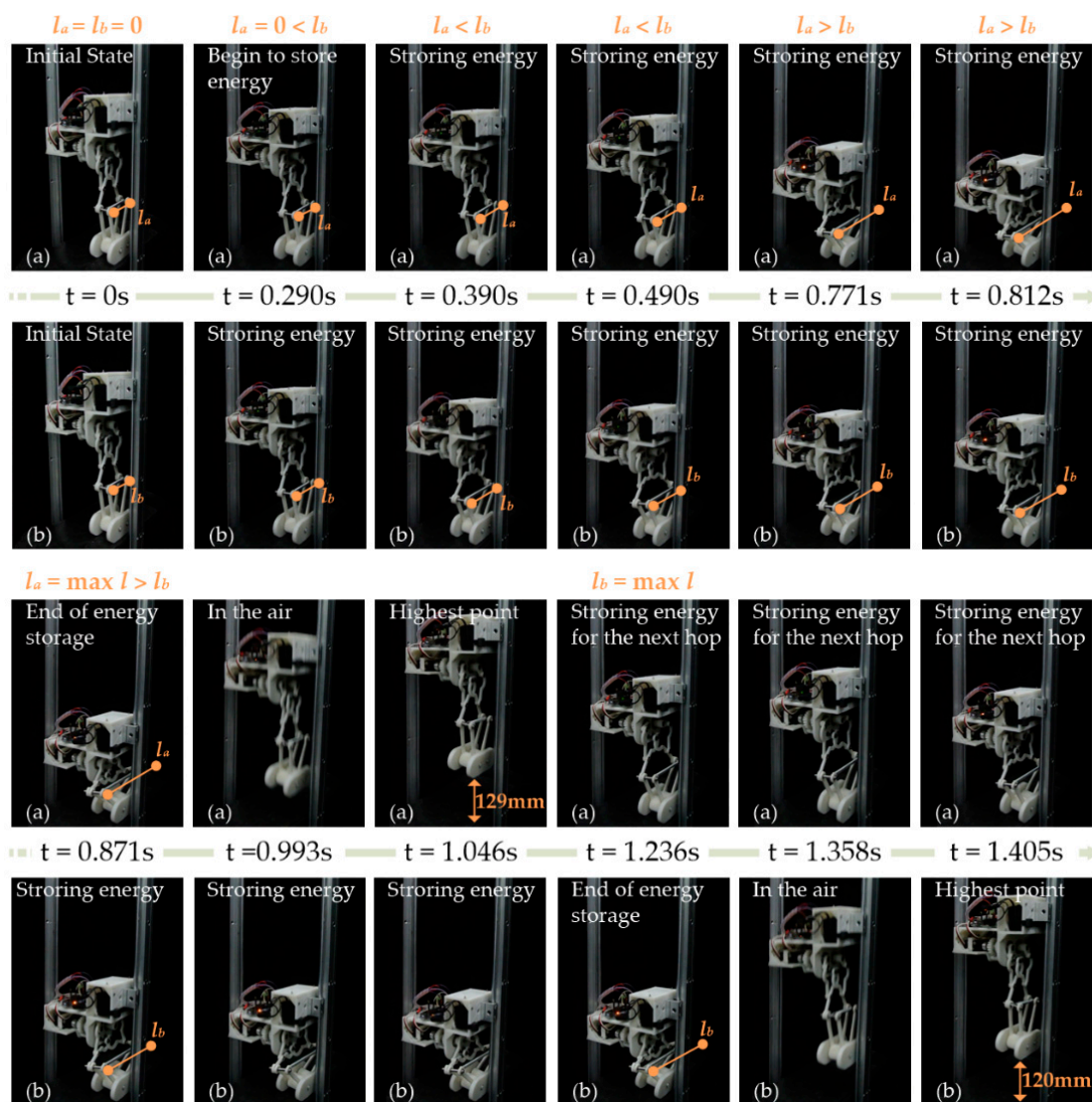


Figure 15. Experimental results comparison for different driving modes. (a) The first prototype equipped with a special actuator; (b) The second prototype equipped with only a rigid motor. l_i means the length of the tension spring.

4.2.3. Continuous Hopping Verification

Figure 16 shows the experimental process of first five continuous hopping cycles within a one hundred hop continuous hopping test. During the experiment, the driving motor rotated continuously in one direction with a constant speed, and the robot hopped repeatedly in the vertical direction along the slide rail until the motor stopped. The time required for the hopping mechanism to complete the first energy storage was about 0.663 s, and the time required for the second and subsequent energy storage was about 0.373 s. The main reason for this is that: after the robot completed the first hopping, each subsequent hopping motion could absorb the partial landing impact energy of the previous hopping, thereby shortening the energy storage time of the next hopping and improving the hopping efficiency and energy utilization.



Figure 16. Experimental process of hopping performance test.

4.3. Comparison With Other Robots

Since the hopping height and the hopping distance differs when the take-off angle of the hopping robot changes, the hopping performance of some state-of-the-art robots were normalized, along with their hopping heights and hopping distances. The specific derivation process of the normalization method is detailed in Appendix B, and the comparison results are shown in Table 4.

As shown in Table 4, RHop performed best in the energy storage speed, which means that when the hopping height is consistent (indicating that the robot is flying in the air for the same time), RHop will complete a hop with less time than other hopping robots (standing on the ground for a shorter time), thereby enhancing its mobility.

Among the existing electrically driven hopping robots, one hopping robot is very special, it is called Salto [3,43,44]. It is driven in the same way as this paper, using more than just a rigid motor. The difference is that the elastic element used in this paper is a clockwork spring, and it uses a solid section of latex, which is also its energy storage component. Using an eight-bar mechanism as a limb with an advanced drive strategy (SEA+MA), Salto has good vertical jumping agility, and can achieve extremely high hops with extremely short standing times. The Salto-1P also adds an attitude control scheme [45,46]. In contrast, the hopping ability of RHop is not as good as that of Salto-1P, but meets both of the requirements mentioned in the paper for the foot trajectory curve and the minimization of the moment acting on the robot's CM when the robot component moves. Salto-1P uses design exploration, combined with kinematic tuning to obtain. Due to the symmetrical nature of its mechanism, RHop does not require any calculations to achieve these requirements, i.e., the exploration process of Salto-1P is more complicated. Additionally, although the control strategy of Salto-1P is

advanced, it is still difficult to control complexity and mechanism coupling. RHop adopts the control mode of continuous circumferential rotation in one direction with constant speed, which is simpler and more operable.

Table 4. Comparison of hopping performance of existing electrically driven robots.

Robot Name	Normalized Hopping Height (m)	Energy Storage Time (s)	Energy Storage Speed (m/s)
Flea-inspired Jumping Robot [47]	0.688	19	0.036
A Jumping Robot [48]	1.071	60	0.018
TAUB [17]	3.335	18.4	0.181
Grillo III [22]	0.125	12.5	0.010
MSU Jumper [31]	0.930	10	0.093
A Bio-inspired Jumping Robot [12]	1.026	60	0.017
A Surveillance Robot [15]	0.410	7.2	0.057
An Integrated Jumping-Crawling Robot [10]	2.900	28	0.104
RHop	0.145	0.373	0.389

5. Conclusion

This paper describes the design and experiment of RHop, a miniaturized continuous hopping robot. Using mechanical evolution, the hopping mechanism in RHop is realized by a geared multi-bar mechanism without an additional locking and releasing mechanism. It is driven by a single motor with continuous circumferential rotation in one direction. It satisfies the proposed DR.1–DR.4, and the optimization results also fulfill the DR.5 and DR.6. The special actuator designed in this paper can amplify the motor torque and reduce the energy storage time, thereby enhancing the overall hopping performance of RHop. Comparative simulations and experiments are conducted for RHop. As the experiments show, the theoretical model, the simulation model, and the prototype are in approximate agreement with each other. In a single hopping, the energy conversion efficiency of RHop reaches a high value of 76.29%. In the continuous hopping experiment, it is proven that a single motor with continuous circumferential rotation in one direction to achieve continuous hopping is feasible. Furthermore, RHop has a good energy storage speed when compared with other state-of-the-art hopping robots.

Future efforts to improve the performance of RHop will include the power matching between the motor and the elastic element, and the coupling and modulating between the special actuator and the tension spring. At the same time, the hopping mechanism that satisfies the design requirements presented in this paper is not unique. The advantages of other combination mechanisms and different design methods can be used to obtain new mechanisms. The design thoughts presented in this paper are still applicable to the exploration of other mechanisms, which will be referenced by other researchers. Additionally, it is also possible to apply the prototype that is developed in this paper to other mobile robots to study multi-mobile robots; particularly, combining this with wheeled movement to improve the obstacle performance could be insightful in improving the environmental adaptability and mobility of the robot.

Supplementary Materials: The following are available online at <http://www.mdpi.com/2076-3417/9/1/13/s1>.

Author Contributions: Conceptualization, L.B., F.Z. and X.C.; Methodology, L.B. and F.Z.; Software, F.Z.; Validation, F.Z. and X.C.; Formal Analysis, L.B. and F.Z.; Investigation, X.C. and J.H.; Resources, L.B. and Y.S.; Data Curation, F.Z. and X.C.; Writing—Original Draft Preparation, L.B.; Writing—Review & Editing, L.B., F.Z., X.C., and Y.S.; Supervision, L.B.; Project Administration, L.B.

Funding: This research was funded by the Foundation for the Sci & Tech Research Project of Chongqing Science & Technology Commission (grant no. cstc2016jcyjA0472, cstc2017zdcy-zdzcX0007, and cstc2015jcyjA70002), the Special Cooperation Program for Higher Education Institutions Collaborative Innovation (grant no. KH2016006), the National Natural Science Foundation of China (grant no. 51505044, 51705050, and 51709023), and the Fundamental Research Funds for the Central Universities (Grant No. 2018CDGFJX0022, 2018CDQYHK0029).

Conflicts of Interest: The authors declare no conflict of interest.

Appendix A

Appendix A.1 D-H Parameter Table

The D-H parameter table of the main and secondary chain mentioned in Section 3.1.1 is shown in the following table.

Table A1. D-H parameter table of the main and secondary chain.

Coordinate System (i)	θ_i	d_i	a_i	α_i
0	-	-	0	0
1	θ_1	0	$l_{P_2P_4}$	0
2	θ_2	0	$l_{P_4P_8}$	0
3	θ_3	0	$l_{P_8P_{10}}$	0
4	θ_4	0	$l_{P_{10}P_{12}}$	0
5	θ_5	0	-	-
1'	$2\pi - \theta_{1'}$	0	$l_{P_2P_6}$	0
2'	$\theta_{2'}$	0	$l_{P_6P_8}$	0
3'	0	0	-	-

Appendix A.2 Constraint Conditions

1. Constraint conditions of the crank-rocker mechanism

According to the conditions for the existence of a crank-rocker mechanism in the planar four-bar linkage $P_2P_4P_8P_6$, the bars l_2, l_3, l_4 , and l_5 have the following six linear constraints:

$$\begin{cases} l_2 - l_i \leq 0 \quad (i = 3, 4, 5) \\ l_2 + l_3 - l_4 - l_5 \leq 0 \\ l_2 + l_4 - l_3 - l_5 \leq 0 \\ l_2 + l_5 - l_3 - l_4 \leq 0 \end{cases} \quad (A1)$$

X represents the 10 dimensions of the optimization design variable, and the 6×10 dimensions matrix A_1 represents the coefficient matrix of the constraint Equation (A1). The six dimensions of vector b_1 represent the constraint vector of Equation (A1), and so Equation (A1) can be changed into:

$$A_1X \leq b_1 \quad (A2)$$

2. Linear constraints of geometric dimensions

According to the requirements of the overall size of the robot, design variables should be restrained, that is:

$$\begin{cases} l_{imin} \leq l_i \leq l_{imax} \quad (i = 1, 2, 3, \dots, 8) \\ \beta_{jmin} \leq \beta_j \leq \beta_{jmax} \quad (j = 1, 2) \end{cases} \quad (A3)$$

The 10 dimensions of vector d_{min} represent the lower-bound matrix of the design variable; the 10 dimensions of vector d_{max} represent the upper-bound matrix of the design variable, then Equation (A3) can be changed into:

$$\begin{cases} X \geq d_{min} \\ X \leq d_{max} \end{cases} \quad (A4)$$

Considering the limitations of processing technology of the component, and the requirement for non-interference of the installation position, the linear constraints of the geometric dimensions are given as:

$$\begin{cases} l_2 - l_1 \leq d_1 \\ l_2 - l_3 \leq d_2 \end{cases} \quad (A5)$$

The 2×10 dimensional matrix A_2 represents the coefficient matrix of the constraint Equation (A5). The two dimensional vector b_2 represents the constraint vector of Equation (A5), so that Equation (A5) can be changed into:

$$A_2X \leq b_2 \tag{A6}$$

3. Non-linear constraints of geometric dimensions

Based on the actual processing requirements of the frame, the limitations of the original length, and the tensile deformation of the tension spring, the following nonlinear constraints exist:

$$\Phi(X) \leq G \tag{A7}$$

where $\Phi(X)$ is a 3-dimensional function vector and G is a 3-dimensional constant vector.

$$\Phi(X) = \begin{pmatrix} \varphi_1(X) \\ \varphi_2(X) \\ \varphi_3(X) \end{pmatrix} = \begin{pmatrix} P_{6x'} \\ P_{9x} - P_{10x} \\ P_{6y'} - P_{9y} \end{pmatrix} \quad G = \begin{pmatrix} g_1 \\ g_2 \\ g_3 \end{pmatrix} = \begin{pmatrix} d_3 \\ d_4 \\ d_5 \end{pmatrix}$$

4. Constraints on the kinematical chain

The main chain and the secondary chain are coupled at the joint P_8 , which means:

$$\begin{cases} h_1(X) = l_2C\theta_1 + l_5C(\theta_{1+2}) - l_3C\theta_{1'} - l_4C(\theta_{1'-2'}) = 0 \\ h_2(X) = l_2S\theta_1 + l_5S(\theta_{1+2}) + l_3S\theta_{1'} + l_4S(\theta_{1'-2'}) = 0 \end{cases} \tag{A8}$$

Point P_6 , P_8 , and P_{10} form a link with three elements, i.e., the slope of the link P_6P_8 and P_8P_{10} are equal:

$$h_3(X) = \frac{S(\theta_{1+2+3})}{C(\theta_{1+2+3})} + \frac{S(\theta_{1'-2'})}{C(\theta_{1'-2'})} = 0 \tag{A9}$$

Since the relative distance between point P_{11} and P_{12} along the X_0 -axis is constant, i.e., there is a constraint relationship $P_{12x} - P_{11x} = l_8$, this means:

$$h_4(X) = 2[l_2C_1 + l_5C_2 + l_6C_3 + l_7C_4] + \frac{1}{2}l_1 - l_8 \tag{A10}$$

where $C_1 = C(\theta_1)$, $C_2 = C(\theta_{1+2})$, $C_3 = C(\theta_{1+2+3})$, $C_4 = C(\theta_{1+2+3+4})$.

Integrating Equation (A8)–(A10), the closed-chain vector constraint of the hopping mechanism is:

$$H(X) = \begin{pmatrix} h_1(X) \\ h_2(X) \\ h_3(X) \\ h_4(X) \end{pmatrix} = 0 \tag{A11}$$

Appendix B

When the take-off angle of a robot is not 90° , let the origin of the coordinate system be at the take-off point, and let the x -axis be along the horizontal direction and the y -axis along the vertical direction. Then, the robot's hopping trajectory can be described as:

$$\begin{cases} x = v_0t \cos \theta \\ y = v_0t \sin \theta - \frac{1}{2}gt^2 \end{cases} \tag{A12}$$

where v_0 is the take-off speed, t is the hopping time, and θ is the take-off angle.

The hopping height h and hopping distance d of the robot can be obtained from Equation (A12):

$$\begin{cases} h = \frac{v_0^2 \sin^2 \theta}{2g} \\ d = \frac{v_0^2 \sin 2\theta}{g} \end{cases} \quad (A13)$$

The normalized hopping height with a take-off angle of 90° is:

$$\begin{cases} \theta = \arctan\left(\frac{4h}{d}\right) (\theta \neq 90^\circ) \\ H = \frac{h}{\sin^2 \theta} \end{cases} \quad (A14)$$

Thus the energy storage speed is:

$$v_s = \frac{H}{T} \quad (A15)$$

where T is the time of the energy storage phase when the robot completes a hop.

According to Equations (A14) and (A15), combined with the hopping height, hopping distance, and energy storage time of the compared robot, the normalized hopping height and energy storage speed of the robot can be calculated, as shown in Table A2.

Table A2. Specific calculation results.

Robot Name	Hopping Height (m)	Hopping Distance (m)	Normalized Hopping Height (m)	Energy Storage Time (s)	Energy Storage Speed (m/s)
Flea-inspired Jumping Robot [47]	0.640	0.700	0.688	19	0.036
A Jumping Robot [48]	1.050	0.600	1.071	60	0.018
TAUB [17]	3.130	3.200	3.335	18.4	0.181
Grillo III [22]	0.100	0.200	0.125	12.5	0.010
MSU Jumper [31]	0.872	0.898	0.930	10	0.093
A Bio-inspired Jumping Robot [12]	1.000	0.650	1.026	60	0.017
A Surveillance Robot [15]	0.410	-	0.410	7.2	0.057
An Integrated Jumping-Crawling Robot [10]	2.900	-	2.900	28	0.104
RHop	0.145	-	0.145	0.373	0.389

References

1. Yoshikawa, K.; Otsuki, M.; Kubota, T.; Maeda, T.; Ushijima, M.; Watanabe, S.; Sakamoto, K.; Kunii, Y.; Umeda, K. A new mechanism of smart jumping robot for lunar or planetary satellites exploration. In Proceedings of the 2017 IEEE on Aerospace Conference, Big Sky, MT, USA, 4–11 March 2017; pp. 1–9.
2. Zhang, Z.; Zhao, J.; Chen, H.; Chen, D. A survey of bioinspired jumping robot: Takeoff, air posture adjustment, and landing buffer. *Appl. Bionics Biomech.* **2017**, *2017*, 1–22. [CrossRef]
3. Plecnik, M.M.; Haldane, D.W.; Yim, J.K.; Fearing, R.S. Design exploration and kinematic tuning of a power modulating jumping monopod. *J. Mech. Robot.* **2017**, *9*, 011009. [CrossRef]
4. Zhu, Y.; Chen, L.; Liu, Q.; Qin, R.; Jin, B. omnidirectional jump of a legged robot based on the behavior mechanism of a jumping spider. *Appl. Sci.* **2018**, *8*, 51. [CrossRef]
5. Ikeda, H.; Kawabe, T.; Wada, R.; Sato, K. Step-climbing tactics using a mobile robot pushing a hand cart. *Appl. Sci.* **2018**, *8*, 2114. [CrossRef]
6. Gart, S.W.; Li, C. Body-terrain interaction affects large bump traversal of insects and legged robots. *Bioinspir. Biomim.* **2018**, *13*, 026005. [CrossRef]
7. Ducros, C.; Hauser, G.; Mahjoubi, N.; Girones, P.; Boisset, L.; Sorin, A.; Jonquet, E.; Falcicola, J.M.; Benhamou, A. RICA: A tracked robot for sampling and radiological characterization in the nuclear field. *J. Field Robot.* **2017**, *34*, 583–599. [CrossRef]
8. Seifert, H.S. The lunar pogo stick. *J. SPACECRAFT* **1967**, *4*, 941–943. [CrossRef]
9. Raibert, M.H.; Tello, E.R. *Legged Robots That Balance*; MIT Press: Cambridge, MA, USA, 1986; p. 89.
10. Burdick, J.; Fiorini, P. Minimalist jumping robots for celestial exploration. *Int. J. Robot. Res.* **2003**, *22*, 653–674. [CrossRef]

11. Dubowsky, S.; Kesner, S.; Plante, J.-S.; Boston, P. Hopping mobility concept for search and rescue robots. *Ind. Robot.* **2008**, *35*, 238–245. [[CrossRef](#)]
12. Wiedebach, G.; Bertrand, S.; Wu, T.; Fiorio, L.; McCrory, S.; Griffin, R.; Nori, F.; Pratt, J. Walking on partial footholds including line contacts with the humanoid robot atlas. In Proceedings of the 2016 IEEE-RAS 16th International Conference on Humanoid Robots (Humanoids), Cancun, Mexico, 15–17 November 2016; pp. 1312–1319.
13. Yan, H.; Li, H.; Zhou, S. Study on hopping height control and detection for the pneumatic actuator. In Proceedings of the 5th International Conference on Electrical Engineering and Automatic Control, Harbin Inst Technol, Weihai, China, 16–18 October 2015; pp. 1121–1128.
14. Graichen, K.; Hentzelt, S.; Hildebrandt, A.; Kärcher, N.; Gaißert, N.; Knubben, E. Control design for a bionic kangaroo. *Control Eng. Practice* **2015**, *42*, 106–117. [[CrossRef](#)]
15. Long, B.; Wenjie, G.; Xiaohong, C.; Qian, T.; Rong, X. Landing impact analysis of a bioinspired intermittent hopping robot with consideration of friction. *Math. Probl. Eng.* **2015**, *2015*.
16. Long, B.; Wenjie, G.; Xiaohong, C.; Meng, X.-y. Hopping capabilities of a bio-inspired and minimally actuated hopping robot. In Proceedings of the 2011 International Conference on Electronics, Communications and Control (ICECC), Ningbo, China, 9–11 September 2011; pp. 1485–1489.
17. Jung, G.-P.; Casarez, C.S.; Jung, S.-P.; Fearing, R.S.; Cho, K.-J. An integrated Jumping-crawling robot using height-adjustable jumping module. In Proceedings of the 2016 IEEE International Conference on Robotics and Automation (ICRA), Stockholm, Sweden, 16–21 May 2016; pp. 4680–4685.
18. Zaitsev, V.; Gvirsman, O.; Hanan, U.B.; Weiss, A.; Ayali, A.; Kosa, G. A locust-inspired miniature jumping robot. *Bioinspir. Biomim.* **2015**, *10*, 066012. [[CrossRef](#)]
19. Jun, B.; Kim, Y.; Jung, S. Design and control of jumping mechanism for a kangaroo-inspired robot. In Proceedings of the 2016 6th IEEE International Conference on Biomedical Robotics and Biomechanics (BioRob), UTown, Singapore, 26–29 June 2016; pp. 436–440.
20. Nguyen, Q.-V.; Park, H.C. Design and demonstration of a locust-like jumping mechanism for small-scale robots. *J. Bionic Eng.* **2012**, *9*, 271–281. [[CrossRef](#)]
21. Zhang, J.; Song, G.; Li, Y.; Qiao, G.; Song, A.; Wang, A. A bio-inspired jumping robot: Modeling, simulation, design, and experimental results. *Mechatronics* **2013**, *23*, 1123–1140. [[CrossRef](#)]
22. Li, F.; Liu, W.; Fu, X.; Bonsignori, G.; Scarfogliero, U.; Stefanini, C.; Dario, P. Jumping like an insect: Design and dynamic optimization of a jumping mini robot based on bio-mimetic inspiration. *Mechatronics* **2012**, *22*, 167–176. [[CrossRef](#)]
23. Song, G.; Yin, K.; Zhou, Y.; Cheng, X. A surveillance robot with hopping capabilities for home security. *IEEE Trans. Consum. Electron.* **2009**, *55*, 2034–2039. [[CrossRef](#)]
24. Wang, H.; Song, G.; Zhang, J.; Meng, T. A Bio-inspired Jumping Robot for Mobile Sensor Networks over Rough Terrain. In *Future Communication, Computing, Control and Management*; Springer: New York, NY, USA, 2012; pp. 57–62.
25. Lambrecht, B.G.A.; Horchler, A.D.; Quinn, R.D. A small, insect-inspired robot that runs and jumps. In Proceedings of the 2005 IEEE International Conference on Robotics and Automation, Barcelona, Spain, 18–22 April 2005; pp. 1240–1245.
26. Sun, Y.; Ge, W.; Zheng, J.; Dong, D. Design and evaluation of a prosthetic knee joint using the geared five-bar mechanism. *IEEE Trans. Neural Syst. Rehabil. Eng.* **2015**, *23*, 1031–1038. [[CrossRef](#)]
27. Sun, Y.; Ge, W.; Zheng, J.; Xia, F.; Dong, D. Optimization of actuating torques in multi-bar prosthetic joints with springs. *Eng. Optimiz.* **2016**, *49*, 1183–1196. [[CrossRef](#)]
28. Zhao, J.; Xi, N.; Gao, B.; Mutka, M.W.; Xiao, L. Design and testing of a controllable miniature jumping robot. In Proceedings of the 2010 IEEE/RSJ International Conference on Intelligent Robots and Systems, Taipei, Taiwan, 18–22 October 2010; pp. 3346–3351.
29. Faraji, H.; Tachella, R.; Hatton, R.L. Aiming and vaulting: Spider inspired leaping for jumping robots. In Proceedings of the 2016 IEEE International Conference on Robotics and Automation (ICRA), Stockholm, Sweden, 16–21 May 2016; pp. 2082–2087.
30. Chan, C.Y.; Liu, Y.C. Towards a walking, turning, and jumping quadruped robot with compliant mechanisms. In Proceedings of the 2016 IEEE International Conference on Advanced Intelligent Mechatronics (AIM), Banff, AB, Canada, 12–15 July 2016; pp. 614–620.

31. Zhao, J.; Jing, X.; Bingtuan, G.; Ning, X.; Fernando, J.C.; Mutka, M.W.; Li, X. MSU Jumper: A Single-Motor-Actuated Miniature Steerable Jumping Robot. *IEEE Trans. Robot.* **2013**, *29*, 602–614. [[CrossRef](#)]
32. Zhao, J.; Yan, W.; Xi, N.; Mutka, M.W.; Xiao, L. A miniature 25 grams running and jumping robot. In Proceedings of the 2014 IEEE International Conference on Robotics and Automation (ICRA), Hong Kong, China, 31 May–7 June 2014; pp. 5115–5120.
33. Freudenstein, F.; Dobrjanskyj, L. On a theory for the type synthesis of mechanisms. In *Applied Mechanics*; Springer: New York, NY, USA, 1966; pp. 420–428.
34. Woo, L.S. Type synthesis of plane linkages. *J. Bionic Eng.* **1967**, *89*, 159.
35. Sun, Y.; Ge, W.; Zheng, J.; Dong, D. Solving the kinematics of the planar mechanism using data structures of assur groups. *J. Mech. Robot.* **2016**, *8*, 061002. [[CrossRef](#)]
36. Buchsbaum, F.; Freudenstein, F. Synthesis of kinematic structure of geared kinematic chains and other mechanisms. *J. Mech. Robot.* **1970**, *5*, 357–392. [[CrossRef](#)]
37. Yokoyama, Y. Studies on the geared linkage mechanisms: 1st report, classification and analysis of geared four-bar linkage. *Bull. JSME* **1974**, *17*, 1332–1339. [[CrossRef](#)]
38. Rocha, C.R.; Tonetto, C.P.; Dias, A. A comparison between the Denavit–Hartenberg and the screw-based methods used in kinematic modeling of robot manipulators. *Comput.-Integr. Manuf.* **2011**, *27*, 723–728. [[CrossRef](#)]
39. Nansai, S.; Rojas, N.; Elara, M.R.; Sosa, R.; Iwase, M. On a Jansen leg with multiple gait patterns for reconfigurable walking platforms. *Adv. Mech. Eng.* **2015**, *7*, 1–18. [[CrossRef](#)]
40. Zelany, M. A concept of compromise solutions and the method of the displaced ideal. *Comput. Oper. Res.* **1974**, *1*, 479–496. [[CrossRef](#)]
41. Hwang, C.L.; Yoon, K. *Multiple Attribute Decision Making*; Springer: New York, NY, USA, 1981; pp. 1–531.
42. Shih, H.S.; Shyur, H.J.; Lee, E.S. An extension of TOPSIS for group decision making. *Math. Comput. Model.* **2007**, *45*, 801–813. [[CrossRef](#)]
43. Haldane, D.W.; Plecnik, M.M.; Yim, J.K.; Fearing, R.S. Robotic vertical jumping agility via series-elastic power modulation. *Sci. Rob.* **2016**, *1*, eaag2048. [[CrossRef](#)]
44. Haldane, D.W.; Plecnik, M.; Yim, J.K.; Fearing, R.S. A power modulating leg mechanism for monopodal hopping. In Proceedings of the 2016 IEEE/RSJ International Conference on Intelligent Robots and Systems (IROS), Daejeon, Korea, 9–14 October 2016; pp. 4757–4764.
45. Haldane, D.W.; Yim, J.K.; Fearing, R.S. Repetitive extreme-acceleration (14-g) spatial jumping with Salto-1P. In Proceedings of the 2017 IEEE/RSJ International Conference on Intelligent Robots and Systems (IROS), Vancouver, BC, Canada, 24–28 September 2017; pp. 3345–3351.
46. Yim, J.K.; Fearing, R.S. Precision Jumping Limits from Flight-phase Control in Salto-1P. In Proceedings of the 2018 IEEE/RSJ International Conference on Intelligent Robots (IROS), Madrid, Spain, 1–5 October 2018.
47. Noh, M.; Kim, S.-W.; An, S.; Koh, J.-S.; Cho, K.-J. Flea-Inspired Catapult Mechanism for Miniature Jumping Robots. *IEEE Trans. Robot.* **2012**, *28*, 1007–1018.
48. Zhang, J.; Song, G.; Qiao, G.; Meng, T.; Sun, H. An Indoor Security System with a Jumping Robot as the Surveillance Terminal. *IEEE Trans. Consum. Electron.* **2011**, *57*, 1774–1781. [[CrossRef](#)]

